A reduced Bloch operator finite element method for fast calculation of elastic complex band structures

A reduced Bloch operator finite element method for fast calculation of elastic complex band structures

Antonio Palermo[a], Alessandro Marzani[a]

[a] *University of Bologna, Department of Civil, Chemical, Environmental and Materials Engineering - DICAM, Bologna, 40136, Italy*

Abstract

This article presents an efficient reduced formulation of the Bloch Operator Finite Element method to calculate complex band structures of periodic waveguides. The use of a Bloch operator formulation allows building and solving a Bloch eigenvalue problem along a generic wave direction, thus being not limited to the unit cell Irreducible Brillouin Zone (IBZ) edges, so that band gap directionality and material absorption in elastic and damped waveguides can be fully disclosed. The proposed Reduced-Order Modelling (ROM) exploits a small set of Bloch modes, extracted at relevant frequency locations along one or more wave directions and post-processed with a Singular Value Decomposition, to reduce the dimensions of the eigenvalue problem. The performances of the proposed numerical technique are evaluated in terms of accuracy and computational saving by analyzing a linear elastic and a damped bi-periodic stubbed plate. Results demonstrate that the reduced formulation yields accurate predictions of propagative, evanescent and complex wave solutions with a reduction in computational time of more than

Email addresses: antonio.palermo6@unibo.it (Antonio Palermo), alessandro.marzani@unibo.it (Alessandro Marzani)

Preprint submitted to International Journal of Solids and Structures December 31, 2019

one order of magnitude with respect to the full model calculations. Complex band structures can thus be efficiently computed over the whole IBZ.
Keywords: Phononic Crystals, Elastic Metamaterials, Floquet-Bloch Theorem, Complex Band Structure, Reduced Order Models

1. Introduction

Natural and engineered media are often characterized by a spatial periodicity, either in their geometry or in the material composition. Such periodicity plays a major role in the the mechanism of propagation of elastic waves, leading to dispersive effects and to the appearance of band gaps, i.e., frequency ranges where mechanical waves are hindered. The presence of these dispersive effects can be predicted by evaluating the material elastic band structure, namely, the relationship between wave vectors and angular frequencies of the mechanical waves supported by the medium. By exploiting the Bloch theorem (Bloch, 1929), the band structure of an infinite periodic system can be evaluated by calculating the vibration modes of a single unit cell. Unit cell vibration modes are extracted by solving an elastodynamic eigenvalue problem (EVP), which is a function of the angular frequency ω and wave vector $\mathbf{k}$ of the waves. Solutions of such ω-$\mathbf{k}$ eigenvalue problem can be obtained for a given $\mathbf{k}$ and an unknown ω, or for a given ω and an unknown $\mathbf{k}$. The $\omega(\mathbf{k})$ EVP is generally solved for real wavenumber selected within the unit cell Irreducible Brillouin Zone (IBZ) and provides the propagative modes, e.g. the real band structure, of the periodic waveguide. Conversely, the $\mathbf{k}(\omega)$ formulation calculates the complex wavenumbers $k = k_r + ik_i$ for given frequency ω, and thus identifies propagative ($k_r \neq 0$, $k_i = 0$), evanescent ($k_r = 0$,

$k_i \neq 0$), and complex ($k_r \neq 0$, $k_i \neq 0$) wave solutions. The identification of evanescent and complex wave solutions is fundamental to capture near-field displacements at the boundaries of a periodic medium (Laude et al., 2011; Kulpe et al., 2014), as well as to predict wave attenuation in band gaps (Laude et al., 2009). Several numerical techniques are currently available to build and solve a Bloch EVP, as the Plane Wave Expansion Method (Sigalas and Economou, 1993; Kushwaha et al., 1993), the Multiple Scattering Method (Sigalas et al., 2005), and the Finite Element Method (Phani et al., 2006; Duhamel et al., 2006; Mace and Manconi, 2008; Hussein, 2009; Collet et al., 2011). In this work, we restrict our attention to Finite Element (FE) based methods, which are popular in solid mechanics thanks to their easiness in implementation, accuracy, convergence and ability in handling complex geometrical domains.

In a FE framework, band structures can be calculated following two different approaches (Hussein et al., 2014). The first one, known as Bloch Operator Finite Element Method (here labelled as BOFEM), assumes a Bloch displacement solution of the elastodynamic problem, builds its weak form utilizing Bloch test functions and discretizes the weak form equation over the unit cell domain using finite elements (Hussein, 2009; Collet et al., 2011). In the second approach, known as Wave Finite Element method (WFEM) (Mace and Manconi, 2008), the unit cell domain is discretized using a standard FE approach and the Bloch theorem is imposed via periodic boundary conditions applied on the unit cell. The use of a BOFEM approach to extract the complex band structure presents some advantages with respect to the WFEM approach. First of all, it allows defining the wave direction where

solutions are sought, preserving the collinearity between imaginary and real part of the wave vector (Collet et al., 2011), a condition that is violated by the WFEM (Mace and Manconi, 2008). Furthermore, it yields a quadratic eigenvalue problem for any considered wave direction of propagation, which can be easily solved by linearization, in contrast to the WFEM that generally yields large non-linear EVPs (see details in the Discussion section) (Mace and Manconi, 2008).

In recent years, several approaches have been developed to reduce the computational effort and accelerate band structures calculation, including among others, multiscale techniques (Hussein and Hulbert, 2006; Casadei et al., 2013, 2016) and the construction of Reduced-Order-Models (ROMs) (Droz et al., 2014; Krattiger and Hussein, 2014; Zhou et al., 2015; Droz et al., 2016; Palermo and Marzani, 2016; Krattiger and Hussein, 2018; Boukadia et al., 2018). The latter approach consists in identifying a basis of coordinates (physical or modal) to reduce the dynamics of a complex system. Two distinct ROM techniques have been so far proposed for band structures calculation within the FE framework. The first technique reduces the dimensions of the unit cell model before imposing the Bloch periodicity by exploiting, for example, the Component Mode Synthesis (CMS) method (Craig and Bampton, 1968). The CMS technique employs a small number of fixed interface modes to replace the internal degree of freedoms (DOFs) of the unit cell, leaving the boundary DOFs untouched and available to impose periodic boundary conditions. Starting from its original implementation restricted to the calculation of real band structures (Krattiger and Hussein, 2014; Zhou et al., 2015), the method has been later extended to calculate complex band

structures (Palermo and Marzani, 2016) and to further reduce its computational cost by means of additional reduction steps (Droz et al., 2016; Krattiger and Hussein, 2018). Unfortunately, the CMS technique cannot be employed to reduce EVPs derived from the BOFEM, since the BOFEM assumes the Bloch periodicity ab initio in the formulation of the operators (Krattiger and Hussein, 2018).

The second ROM technique employs a reduced modal-basis to project the matrix operators of the Bloch EVP. An example of this approach is given in Ref. (Droz et al., 2014), where a small set of shape functions associated to propagating waves is exploited to reduce the WFEM EVP and calculate the real band structure of 1D waveguides. The procedure utilizes a basis of positive-going waves extracted at multiple cut-on frequencies of the analyzed waveguide. The correlation between the selected wave shapes is evaluated by using a Modal Assurance Criterion (MAC), which allows to discriminate least correlated modes by assessing their degree of correspondence (further details on the method can be found in Ref. (Allemang, 2003).

More recently, the approach has been updated to span the full complex band structure by introducing a further wavenumber sampling procedure and implementing a Singular Value Decomposition step (Boukadia et al., 2018), for a more robust selection of uncorrelated modes. Given the ability of this method to reduce the computational burden of the WFEM formulation, it is desirable to borrow some of its numerical techniques and adapt its application to the BOFEM, so to exploit its advantages with respect to WFEM formulations and calculate complex band structures along generic wave directions. Indeed, current reduction techniques for the BOFEM are limited

to the Reduced Bloch Mode Expansion (RBME) method (Hussein, 2009), which exploits a reduced basis of propagative Bloch eigenfunctions, selected at the high-symmetry points of the unit cell IBZ, to obtain an accurate approximation of the waveguide real band structures.

Hence, in this work we propose a reduced formulation for BOFEM to calculate complex band structures in periodic media. The method builds a reduced dimension Bloch EVP along a single or along multiple wave directions selected within the IBZ. In particular, two reduction strategies are presented and discussed in details. The first, named as single-direction (SD) reduction, exploits a basis of wave shapes extracted along the same direction where the Bloch EVP is set and solved. The second, named as multi-direction (MD) reduction, builds a set of basis along predefined wave directions later used to project the EVP within the full IBZ.

The paper is organized as follow. In section 2, the BOFEM is reviewed and its formulation is discussed in details for both the $\omega(\mathbf{k})$ and the $\mathbf{k}(\omega)$ approaches. In section 3, we present the proposed reduction strategies, providing a detailed implementation of the single and multi-direction reductions for a bi-periodic 3D waveguide. Then, the accuracy and computational saving of the procedures are discussed by computing the complex band structures of a stubbed plate (section 4). First, the performance of the reduced models is evaluated for the case of a linear elastic stubbed plate. Then, reduced models are developed for the case of a damped stubbed plate. In both cases, accuracy and computational cost of the methods are discussed for complex band structures calculated along a specific wave direction and within the whole IBZ. Finally, a discussion on the performance of the proposed reduction with

respect to available ROM techniques is given in section 5. Concluding remarks are drawn is section 6.

2. Overview of the Bloch operator FE method

In this section, we review the BOFEM as originally proposed by Collet et al. in Ref. (Collet et al., 2011).

2.1. Strong formulation of the elastic Bloch eigenvalue problem

Let us consider a generic infinite periodic elastic medium as the one shown in Fig. 1a, whose dynamic equilibrium equations read:

$$\rho(\mathbf{x})\omega^2\mathbf{u}(\mathbf{x}) + \nabla\cdot\mathbf{C}(\mathbf{x}) : \nabla^S\mathbf{u}(\mathbf{x}) = \mathbf{0}, \qquad \mathbf{x}\in\mathbf{R}^3 \tag{1}$$

where $\rho(\mathbf{x})$ is the mass density, ω the angular frequency, $\mathbf{C}(\mathbf{x})$ the elastic Hook tensor, $\mathbf{u}(\mathbf{x})$ the displacement vector and $\boldsymbol{\epsilon}(\mathbf{x})=\nabla^S\mathbf{u}(\mathbf{x}) = 1/2(\nabla\mathbf{u}(\mathbf{x})+(\nabla\mathbf{u}(\mathbf{x}))^T)$ the strain tensor. We restrict our analysis to the unit cell of the periodic medium, identified by the domain Ω_R (see Fig. 1b). By invoking the Bloch theorem (Bloch, 1929), eigensolutions of the elastodynamic problem in Eq. (1) defined over the unit cell domain Ω_R, are sought in the form:

$$\mathbf{u}(\mathbf{x}) = \mathbf{u}_n(\mathbf{x},\mathbf{k})e^{-i\mathbf{k}\mathbf{x}} \tag{2}$$

where $\mathbf{k}=[k_x,k_y,k_z]^T$ is the wave vector and $\mathbf{u}_n(\mathbf{x},\mathbf{k})$ are periodic functions in Ω_R, $\mathbf{x}\in\Omega_R$ (see Fig. 1c). Substituting Eq. (2) in Eq. (1) leads to a generalized eigenvalue problem:

$$\begin{aligned}\rho(\mathbf{x})\omega_n^2(\mathbf{k})\ \mathbf{u}_n(\mathbf{x}) + \nabla\cdot\mathbf{C}(\mathbf{x}) : \nabla^S\mathbf{u}_n - i\mathbf{C}(\mathbf{x}) : \nabla^S\mathbf{u}_n\cdot\mathbf{k}\\ -i\nabla\cdot\mathbf{C}(\mathbf{x}) : \frac{1}{2}(\mathbf{u}_n(\mathbf{x})\otimes\mathbf{k}+\mathbf{k}\otimes\mathbf{u}_n(\mathbf{x}))\\ +\mathbf{C}(\mathbf{x}) : \frac{1}{2}(\mathbf{u}_n(\mathbf{x})\otimes\mathbf{k}+\mathbf{k}\otimes\mathbf{u}_n(\mathbf{x}))\cdot\mathbf{k} = \mathbf{0}, \qquad \mathbf{x}\in\Omega_R\end{aligned} \tag{3}$$

with symmetrical boundary conditions defined on the unit cell boundary faces Γ_R:

$$\mathbf{u}_n(\mathbf{x} - \mathbf{R} \cdot \mathbf{n}) - \mathbf{u}_n(\mathbf{x}) = 0, \qquad \mathbf{x} \in \Gamma_R, \tag{4}$$

where $\mathbf{R} = [\mathbf{r}_x, \mathbf{r}_y, \mathbf{r}_z]$ is the matrix of the lattice vectors and $\mathbf{n}$ is the unit outpointing normal vector defined on the considered boundary.

Eq. (3) is the strong form of a generalized EVP in the variables ω and $\mathbf{k}$. The wave vector $\mathbf{k}$ can be rearranged as the product of its amplitude $|\mathbf{k}|$ and the vector of cosine direction $\mathbf{\Phi}$ (see Fig. 1c):

$$\mathbf{k} = |\mathbf{k}|\mathbf{\Phi} = |\mathbf{k}| \begin{bmatrix} \cos\theta\cos\phi \\ \cos\theta\sin\phi \\ \sin\theta \end{bmatrix} \tag{5}$$

As a result, the EVP in Eq. (3) depends on three variables, namely the angular frequency ω, the wave vector amplitude $|\mathbf{k}|$, and the wave direction $\mathbf{\Phi}$.

2.2. Weak form and FE discretization

By projecting Eq. (3) onto a Bloch periodic test function $\tilde{\mathbf{u}}_n(\mathbf{x})$ defined over the unit cell domain Ω_r, and by integrating this projection over the same domain, a weak form of the EVP is obtained (all the details can be found in Ref. (Collet et al., 2011)). A numerical implementation of the weak form is then obtained by using a standard FE discretization, which yields the set of equations:

$$[\mathbf{K} + \lambda\mathbf{L}(\mathbf{\Phi}) - \lambda^2\mathbf{H}(\mathbf{\Phi}) - \omega_n^2(\lambda, \mathbf{\Phi})\mathbf{M}]\mathbf{u}_n(\mathbf{\Phi}) = \mathbf{0}. \tag{6}$$

In Eq. (6) the reader can find the standard mass and stiffness matrix, $\mathbf{M}$ and $\mathbf{K}$ respectively, a skew-symmetric matrix $\mathbf{L}$ and a symmetric semi-definite

positive matrix $\mathbf{H}$:

$$
\begin{aligned}
\mathbf{K} &= \int_{\Omega_r} \boldsymbol{\epsilon}_n(\mathbf{x})\mathbf{C}(\mathbf{x})\tilde{\boldsymbol{\epsilon}}_n(\mathbf{x})\partial\Omega, \\
\mathbf{M} &= \int_{\Omega_r} \rho(\mathbf{x})\mathbf{u}_n(\mathbf{x})\tilde{\mathbf{u}}_n(\mathbf{x})\partial\Omega, \\
\mathbf{L} &= \int_{\Omega_r} (-\tilde{\boldsymbol{\kappa}}_n(\mathbf{x})\mathbf{C}(\mathbf{x})\boldsymbol{\epsilon}_n(\mathbf{x}) + \tilde{\boldsymbol{\epsilon}}_n(\mathbf{x})\mathbf{C}(\mathbf{x})\boldsymbol{\kappa}_n(\mathbf{x}))\partial\Omega, \\
\mathbf{H} &= \int_{\Omega_r} \tilde{\boldsymbol{\kappa}}_n(\mathbf{x})\mathbf{C}(\mathbf{x})\boldsymbol{\kappa}_n(\mathbf{x})\partial\Omega.
\end{aligned}
\tag{7}
$$

where $\lambda = ik = i(k_r + ik_i)$, $\boldsymbol{\epsilon}_n(\mathbf{x})$ is the strain tensor and $\boldsymbol{\kappa}_n = 1/2(\mathbf{u}_n \otimes \boldsymbol{\Phi} + (\mathbf{u}_n \otimes \boldsymbol{\Phi})^T)$ is the symmetric dyadic product of the displacement $\mathbf{u}_n(\mathbf{x})$ and the direction vector $\boldsymbol{\Phi}$. By solving Eq. (6) with given real wavenumbers $\lambda = ik_r$ along the direction $\boldsymbol{\Phi}$, a linear eigenvalue problem with ω_n^2 as unknown is obtained, namely a $\omega(k_r)$ EVP, whose solutions are sought within the unit cell IBZ. In addition, Eq.(6) can be formulated as:

$$
[(\mathbf{K} - \omega^2\mathbf{M}) + \lambda_n(\omega, \Phi)\mathbf{L}(\boldsymbol{\Phi}) - \lambda_n^2(\omega, \Phi)\mathbf{H}(\boldsymbol{\Phi})]\mathbf{u}_n(\boldsymbol{\Phi}) = \mathbf{0} \tag{8}
$$

where λ_n and the associated eigenvectors $\mathbf{u}_n$ are computed for given real frequency ω. Such an approach, namely a $k(\omega)$ EVP, allows the calculation of complex band structures ($k_{r,n}(\omega)$ and $k_{i,n}(\omega)$) along the generic wave direction. We remind that the quadratic EVP is solved via linearization, yielding a solving system of dimensions $(2n \times 2n)$.

As discussed in the introduction, ROM techniques for BOFEM are currently limited to the calculation of the real band structures (Hussein, 2009), making the methodology less appealing for large computational problems and for parametric design of phononic materials and metamaterials. Hence, in the next section we introduce and discuss a model reduction methodology for

complex band structures calculation via BOFEM.

3. Proposed reduction strategy

The fundamental steps of the proposed ROM procedure are presented in Fig. 2 and summarized below:

1. identification of unit cell IBZ and definition of a set of wave directions;
2. calculation of cut-on and termination frequencies at each wave direction using Eq. (6);
3. extraction of eigenvalues λ_n at the cut-on and termination frequencies using Eq. (8) and selection of propagative and (least) evanescent solutions for the wave basis;
4. construction of a projection matrix from single-direction and multiple directions wave basis using the Singular Value Decomposition;
5. solution of the reduced $k(\omega)$ EVP for complex band structures extraction and directivity analysis of linear elastic and damped periodic media.

In what follows, we describe in details all the steps of the proposed reduction. The procedure is presented for a bi-periodic material but can be easily translated to the 3D periodic case.

3.1. Identification of unit cell IBZ and definition of a set of wave directions

Let us consider a bi-periodic unit cell, with a rectangular Bravais lattice of dimensions $a_x \times a_y$ (Fig. 3). We start by identifying the unit cell FBZ, i.e, the domain $\Omega_g = [-\pi/a_x : \pi/a_x, -\pi/a_y : \pi/a_y]$ defined in the reciprocal lattice space. Solutions with real wavenumbers outside the FBZ are

discarded both in the wave-basis extraction procedure (step 3) and in the reduced band structure calculation (step 5). Similarly, the range of possible wave directions required to investigate the dynamics and directivity of the medium are bounded by dimensions of the IBZ. In this regard, care should be taken when unit cells with low order symmetries are studied (Maurin et al., 2018), since their IBZ can significantly change with respect to that of high symmetric unit cells (see Fig. 3b for a comparison between a high and a low symmetry unit cell IBZ). Once the IBZ is identified, a set of wave directions:

$$\mathbf{\Phi}_j = \begin{bmatrix} \cos\theta_j \\ \sin\theta_j \\ 0 \end{bmatrix}, \quad \theta_j = \theta_1, ..., \theta_d \tag{9}$$

is selected to construct the wave basis (further details are given in Sect. 3.4).

3.2. Calculation of cut-on and termination frequencies

Cut-on frequencies, i.e. angular frequencies $\omega_{c,n}$ calculated for $k_r = 0$, are interesting points in the dynamics of a waveguide, since they mark the progressive appearance of higher modes supported by the medium (Droz et al., 2014). Similar arguments apply to the termination frequencies, namely angular frequencies $\omega_{t,n}$ at $k_r = k_{r,max}$ along $\mathbf{\Phi}_j$, since they can identify the cut-off of wave modes and the edges of frequency band gaps in the band structures of phononic crystals and metamaterials. Hence, a sampling strategy of the wave basis at these locations allows to capture all the relevant changes in the wave shapes and in the frequency spectrum of the waveguide.

Cut-on frequencies are independent from the wave propagation direction, and are calculated once during the model reduction procedure. For the cal-

culation of cut-on frequencies $\omega_{c,n}(\lambda = 0)$, the EVP in Eq. (6) simplifies as:

$$[\mathbf{K} - \omega_{c,n}^2 \mathbf{M}]\mathbf{u}_n = \mathbf{0} \tag{10}$$

Conversely, termination frequencies are calculated from Eq. (6) and considering a value of the real wavenumber lying the edge of the IBZ along the wave direction $\mathbf{\Phi}_j$ ($\lambda_j^{max} = ik_{r,j}^{max}$):

$$[\mathbf{K} + \lambda_j^{max}\mathbf{L}(\mathbf{\Phi}_j) - (\lambda_j^{max})^2\mathbf{H}(\mathbf{\Phi}_j) - \omega_{t,n}^2(\lambda_j^{max}, \mathbf{\Phi}_j)\mathbf{M}]\mathbf{u}_n(\mathbf{\Phi}_j) = \mathbf{0}. \tag{11}$$

As a result, for each direction $\mathbf{\Phi}_j$, a set of sampling frequencies $\Omega_{s,j} = [\omega_{1,j}, ..., \omega_{s,j}]$, collecting cut-on and termination frequencies up to the maximum frequency of interest, is assembled. We remind that when dissipation is accounted in the material, complex frequencies $\omega^* = \omega_r + i\omega_i$ are found. Nonetheless, minor changes in the frequency spectrum are introduced by moderate values of material damping (Moiseyenko and Laude, 2011; Krushynska et al., 2016). Hence, in the proposed procedure, only the real parts of the sampled frequencies ω_r are stored and later used as input for the definition of the reduced basis.

3.3. Extraction of Floquet-Bloch eigenvectors at the sampling frequency set

Once the frequency subset $\Omega_{s,j}$ is defined, the wave basis $\boldsymbol{\Psi} = [\boldsymbol{\psi}_{n,1}, ..., \boldsymbol{\psi}_{n,s}]$ for the direction $\boldsymbol{\Phi}_j$ is constructed by solving s EVPs :

$$\begin{cases} [(\mathbf{K} - \omega_{1,j}^2\mathbf{M}) + \lambda_{n,1}(\omega_{1,j}, \boldsymbol{\Phi}_j)\mathbf{L}(\boldsymbol{\Phi}_j) - \lambda_{n,1}^2(\omega_{1,j}, \boldsymbol{\Phi}_j)\mathbf{H}(\boldsymbol{\Phi}_j)]\boldsymbol{\psi}_{n,1}(\boldsymbol{\Phi}_j) = \mathbf{0} \\ [(\mathbf{K} - \omega_{2,j}^2\mathbf{M}) + \lambda_{n,2}(\omega_{2,j}, \boldsymbol{\Phi}_j)\mathbf{L}(\boldsymbol{\Phi}_j) - \lambda_{n,2}^2(\omega_{2,j}, \boldsymbol{\Phi}_j)\mathbf{H}(\boldsymbol{\Phi}_j)]\boldsymbol{\psi}_{n,2}(\boldsymbol{\Phi}_j) = \mathbf{0} \\ \vdots \\ [(\mathbf{K} - \omega_{s,j}^2\mathbf{M}) + \lambda_{n,s}(\omega_{s,j}, \boldsymbol{\Phi}_j)\mathbf{L}(\boldsymbol{\Phi}_j) - \lambda_{n,s}^2(\omega_{s,j}, \boldsymbol{\Phi}_j)\mathbf{H}(\boldsymbol{\Phi}_j)]\boldsymbol{\psi}_{n,s}(\boldsymbol{\Phi}_j) = \mathbf{0} \end{cases} \tag{12}$$

As suggested in Ref. (Droz et al., 2014), from the full set of eigensolutions $\lambda_{n,s}$ and related eigenmodes $\boldsymbol{\psi}_{n,s}$, we select only l positive-going waves (i.e., $l << n \times s$), with a desired amplitude attenuation:

$$\boldsymbol{\psi}_{n,s}(\boldsymbol{\Phi}_j) \in \boldsymbol{\Psi}(\boldsymbol{\Phi}_j) \quad \text{if} \quad \begin{cases} 0 \leq \Re(k_{n,s}) \leq k_{r,j}^{max} \\ |\Im(k_{n,s})| < \alpha k_{r,j}^{max} \end{cases} \tag{13}$$

Large values of the parameter α yield a large number of complex and evanescent modes retained in the wave-basis, for an accurate calculation of the amplitude decay in the band gap. In our study, we adopt a parameter $\alpha = 1$ to select evanescent and complex modes with an amplitude decay per unit cell length L_j along the direction $\boldsymbol{\Phi_j}$ equal to $A_{d,j} = e^{k_{r,j}^{max} L_j}$.

Following the suggestions in Ref. (Droz et al., 2014), the numerical stability of the reduction procedure is improved by forming a doubled size (i.e., $2 \times l$) wave basis composed by the real and imaginary components of the selected complex eigenmodes as:

$$\boldsymbol{\Psi}(\boldsymbol{\Phi}_j)^* = [\Re(\boldsymbol{\Psi}(\boldsymbol{\Phi}_j)) \quad \Im(\boldsymbol{\Psi}(\boldsymbol{\Phi}_j))]. \tag{14}$$

Finally, r rigid modes $\boldsymbol{\psi}_{r,0}$, extracted from the EVP ($\omega = 0$):

$$[\mathbf{K} + \lambda_{n,0}\mathbf{L}(\boldsymbol{\Phi}_j) - \lambda_{n,0}^2\mathbf{H}(\boldsymbol{\Phi}_j)]\boldsymbol{\psi}_{n,0}(\boldsymbol{\Phi}_j) = \mathbf{0} \tag{15}$$

are added to the basis to correctly capture the quasi-static and low frequency behavior of the waveguide. As a result a collection of ($m = 2 \times l + r$) vectors is retained to form the wave basis $\boldsymbol{\Phi}_j$.

3.4. Construction of a projection matrix from single-direction and multiple-direction wave basis

3.4.1. Single-direction EVP reduction

Following the approach in Ref. (Boukadia et al., 2018), we perform a Singular Value Decomposition of the ($n \times m$) wave-basis $\boldsymbol{\Psi}(\boldsymbol{\Phi}_j)^*$. The SVD is performed to further reduce the possibility of numerical instabilities induced by the presence of redundant vectors in $\boldsymbol{\Psi}(\boldsymbol{\Phi}_j)^*$. The SVD leads to the identification of three matrices:

$$\boldsymbol{\Psi}(\boldsymbol{\Phi}_j)^* = \mathbf{U}^\mathbf{T}\boldsymbol{\Sigma}\mathbf{V} \tag{16}$$

In Eq. (16), $\mathbf{U}$ is an ($n \times n$) complex unitary matrix, $\boldsymbol{\Sigma}$ is an ($m \times n$) rectangular diagonal matrix with non-negative real numbers on the diagonal, and $\mathbf{V}$ is an ($m \times m$) complex unitary matrix. The diagonal entries σ_i of $\boldsymbol{\Sigma}$ are the singular values of $\boldsymbol{\Psi}(\boldsymbol{\Phi}_j)^*$. The columns of the matrices $\mathbf{U}$ and $\mathbf{V}$ are the left-singular vectors and right-singular vectors of the matrix $\boldsymbol{\Psi}(\boldsymbol{\Phi}_j)^*$, respectively.

The projection matrix $\mathbf{P}(\boldsymbol{\Phi}_j)$ is thus formed by collecting p left-singular vectors, (e.g, p columns of the matrix $\mathbf{U}$) corresponding to the p largest

non-null diagonal entries of the matrix $\mathbf{\Sigma}$, i.e., the largest singular values of $\mathbf{P}(\mathbf{\Phi}_j)$. The truncation criterion on the largest singular values is given as:

$$\frac{\sum_{i=1}^{p} \sigma_i}{\sum_{j=1}^{m} \sigma_j} = 1 - \beta \tag{17}$$

where β can be chosen according to the accuracy and computational cost reduction desired. As a result, an $(n \times p)$ projection matrix $\mathbf{P}(\mathbf{\Phi}_j)$ is built. A reduced EVP defined along the direction $\mathbf{\Phi}_j$, for the frequency ω, and projected on a basis of left-singular vectors $\mathbf{P}(\mathbf{\Phi}_j)$ is obtained as:

$$[(\hat{\mathbf{K}} - \omega^2 \hat{\mathbf{M}}) + \lambda_n(\omega, \mathbf{\Phi}_j)\hat{\mathbf{L}}(\mathbf{\Phi}_j) - \lambda_n^2(\omega, \mathbf{\Phi}_j)\hat{\mathbf{H}}(\mathbf{\Phi}_j)]\hat{\boldsymbol{\psi}}_n(\mathbf{\Phi}_j) = \mathbf{0} \tag{18}$$

where:

$$\begin{aligned} \hat{\mathbf{K}} &= \mathbf{P}^{\mathbf{T}}(\mathbf{\Phi}_j)\mathbf{K}\mathbf{P}(\mathbf{\Phi}_j) \\ \hat{\mathbf{M}} &= \mathbf{P}^{\mathbf{T}}(\mathbf{\Phi}_j)\mathbf{M}\mathbf{P}(\mathbf{\Phi}_j) \\ \hat{\mathbf{L}} &= \mathbf{P}^{\mathbf{T}}(\mathbf{\Phi}_j)\mathbf{L}\mathbf{P}(\mathbf{\Phi}_j) \\ \hat{\mathbf{H}} &= \mathbf{P}^{\mathbf{T}}(\mathbf{\Phi}_j)\mathbf{H}\mathbf{P}(\mathbf{\Phi}_j) \end{aligned} \tag{19}$$

are reduced $(p \times p)$ matrices. In what follows, we refer to the projection matrix $\mathbf{P}(\mathbf{\Phi}_j)$ as a single-direction (SD) projection matrix, since it is built utilizing a wave-basis collinear with the direction of the EVP.

3.4.2. Multi-direction EVP reduction

As discussed in Sect. 2, the BOFEM allows evaluating the band structure of a periodic medium along any wave direction without increasing the complexity of the EVP formulation. For this reason, the method is particularly suitable to analyse the directivity of a periodic medium, to identify directional band gaps within the IBZ and to quantify material absorption along specific directions when damping is taken into account.

When the full IBZ is investigated along j wave directions, the SD reduction requires the construction of j wave-basis and projection matrices. A further improvement on the reduction procedure computational savings can be achieved by projecting the EVP along a reduced set of non-collinear wave-basis. In more details, for a bi-periodic waveguide whose IBZ spans the wave direction range $\Theta = [\theta_0 - \theta_{end}]$, we build the projection matrices $\mathbf{P}(\mathbf{\Phi}_d)$ along a reduced set of directions $\Theta_d = [\theta_0, ..., \theta_d, ..., \theta_{end}]$, following for each direction θ_d the procedure described in Sect. 3.4.1. Then, each EVP along a generic direction $\theta_j \in [\theta_d, \theta_{d+1}]$ is reduced by employing a unique multi-direction (MD) projection matrix:

$$\mathbf{P}(\mathbf{\Phi}_{d,d+1}) = [\mathbf{P}(\mathbf{\Phi}_d) \quad \mathbf{P}(\mathbf{\Phi}_{d+1})] \tag{20}$$

where $\mathbf{P}(\mathbf{\Phi}_{d,d+1})$ concatenates $p_d + p_{d+1}$ left-singular vectors, selected respectively along the directions θ_d and θ_{d+1}.

As a result, when the band structures are evaluated along j wave directions within the IBZ, only $d << j$ projection matrices are constructed. Accuracy and computational savings of the presented single-direction and multi-direction reduction strategies are discussed in the following section.

4. Case study

The performance of the proposed reduction schemes is evaluated by calculating the complex band structures of the bi-periodic waveguide shown in Fig. 4a. This stubbed plate, originally proposed by Wu et al. (Wu et al., 2009, 2008), has been later employed to discuss the BOFEM (Collet et al., 2011) and the EBMS reduction for the WFEM approach (Palermo and Marzani,

2016). The waveguide consists of an aluminum plate of thickness t=1 mm decorated with cylindrical stubs of height h_s=5 mm and radius r_s=3.5 mm, placed over the plate surface to form a square array of lattice constant a= 10 mm. The material is assumed to be isotropic with density ρ=2700 kg/m^3, Young's modulus E=69 GPa and Poisson's ratio ν=0.33. The unit cell FBZ is shown in Fig. 4b, with the related IBZ highlighted in blue. The BOFEM is implemented in Comsol Multiphysics, while the reduction procedure is developed via Matlab routines.

4.1. Undamped Plate

The complex band structures of an undamped linear elastic stubbed plate are here presented to discuss the accuracy of the proposed SD and MD reductions. As in Ref. (Collet et al., 2011), computations are carried for 201 frequencies between 0 and 200 kHz (i.e., a frequency point for each kHz). The plate unit cell is discretized using Lagrange tetrahedral quadratic elements for a mesh of 13581 degrees of freedom (see Fig. 4c), adequate to accurately capture the dynamics of the unit cell within the frequency range of interest. Before analyzing the accuracy of the reduction procedure, we quickly review the dynamics of the periodic plate, according to the results provided by the BOFEM (Collet et al., 2011) (black circles in Fig. 5 a,b). First, we evaluate the complex band structure along the generic wave direction $\theta_j = \pi/10$. The band structure presents three band gaps BG_i, i=1,2,3, highlighted in light blue in Fig. 5. The band gap BG_1 spans the frequency range between $40 - 50$ kHz, the BG_2 the frequencies between $110 - 116$ kHz, the BG_3 between $150 - 182$ kHz. All the BGs arise from the coupling between the plate dynamics and the stubs resonances. As regards to the adopted

computational model, the propagative modes extracted with the $k(\omega)$ EVP in Eq.(8) fully agree with the real band structure (continuous gray lines in Fig. 5a) calculated by means of the $\omega(k)$ approach of Eq.(6). Together with propagative solutions, the $k(\omega)$ EVP provides also evanescent and complex modes, which are displayed in Fig. 5b, for a maximum value of the imaginary wavenumber $k_i = k_{r,max} = 330.32$ rad/m. The evanescent and complex modes define the dynamics of the periodic medium within the BGs as well as the near field solutions which arise at the interfaces or boundaries of a finite size periodic media. Given the multitude of evanescent and complex solutions found within the range $k_i = k_{r,max}$, a compact representation of the wave amplitude decay of a periodic medium can be given by utilizing the minimal evanescent index $E_{ind}(\omega)$ (Collet et al., 2011):

$$E_{ind}(\omega) = \min_n \frac{k_{i,n}}{{k_{i,n}}^2 + {k_{r,n}}^2} \tag{21}$$

which measures the minimal amplitude attenuation across the frequency spectrum of interest. As expected, for an undamped plate, non-null values of $E_{ind}(\omega)$ are found only within the BGs (see Fig. 5c).

Let us now discuss the accuracy and the computational time reduction of the proposed SD and MD ROM techniques. For the SD reduction, a subset of cut-on and termination frequencies is selected along the direction of computation $\theta = \pi/10$ up to the maximum frequency of interest $f_{max} = 200$ kHz. Then, Bloch eigenmodes are extracted according to Eq. (12). Following the procedure in section 3.3, we select propagative and least decaying modes ($\alpha = 1$ in Eq.(13)) at cut-on and termination frequencies $< f_{max}$. We then post-process these Bloch modes with the SVD, and select the related left-singular vectors according the truncation criterion in Eq. (17), setting a

$\beta = 10^{-6}$. The procedure results in a SD projection matrix composed by 89 left-singular vectors.

For the MD reduction, the same procedure is performed twice (utilizing the same $\beta = 10^{-6}$), along the direction $\theta_1 = 0$, $\theta_2 = \pi/8$, respectively, leading to a MD projection matrix of 158 left-singular vectors (note that the directions where the projection matrices are built do not include the direction of computation $\theta = \pi/10$). The matrices are then used to reduce the EVP and replicate the complex band structure of the full model. As for the full model, the band structure is presented separately for propagative (Fig. 5a) and for evanescent and complex solutions (Fig. 5b). Fig. 5a presents very good visual agreement between the full and reduced SD (blue "x" markers) and MD (red "+" markers) real band structures. A similar qualitative agreement is observed in the prediction of complex and evanescent solutions (Fig. 5b) and in the related $E_{ind}(\omega)$ (Fig. 5c). We perform a quantitative analysis on the accuracy of the model reduction across the frequency range of interest by calculating the maximum discrepancy in the prediction of the real wavenumber components:

$$e_{k_r}(\omega) = \max_n \left| \frac{k_{r,n}^{Full}(\omega) - k_{r,n}^{Red}(\omega)}{k_{r,n}^{Full}(\omega)} \right| \tag{22}$$

where $k_{r,n}^{Full}(\omega)$ and $k_{r,n}^{Red}(\omega)$ are the real part of the n wavenumbers calculated using the full and reduced (either SD or MD) models, respectively. Similarly, we evaluate the maximum discrepancy in the minimal evanescence index calculation:

$$e_{E_{Ind}}(\omega) = \left| \frac{E_{Ind}^{full}(\omega) - E_{Ind}^{Red}(\omega)}{E_{Ind}^{full}(\omega)} \right| \tag{23}$$

The two error indices, Eqs. (22)-(23), are shown in Fig. 6a and 6b, respectively. Inspection of Fig. 6a highlights that the maximum discrepancy e_{k_r} in the frequency ranges far from the BGs edges is generally below 10^{-4} for the SD reduction and below 10^{-2} for the MD reduction, respectively. Peak of discrepancies are found at the edges of the BGs where flat branches exist. This occurs because the ROM techniques lead to "stiffer" numerical models which over-predict the vibration frequencies of the unit cell. Such small shift in the frequency prediction determines a large shift in the wavenumber calculation when flat branches are predicted. Indeed, the same peak discrepancies are observed in WFEM-based ROM techniques (Palermo and Marzani, 2016; Krattiger and Hussein, 2018). As expected, the SD reduction presents a higher accuracy with respect to the MD thanks to the use of a collinear wave-basis. Nonetheless, the accuracy of the MD reduction can be still considered adequate for analysis and design purposes. In this regards, the reader can refer to the average values of the discrepancy calculated within the whole frequency range of interest and collected in Table 1. Similar trends are found for E_{ind}, provided only within the BGs, where the index assumes non-null values.

As regards to the computational cost of the reduction procedures, Table 1 compares the total time required for the band structures calculation with the full and reduced models, as well as the computational times of each step of the reductions. The calculations are performed on a machine equipped with a Intel i76600U CPU @ 2.6 GHz with a RAM of 16 GB. The computational time of the full model solution $t_{full} \approx 40$ min, needed to solve the 201 full EVPs, drops to $t_{SD} \approx 4$ min and $t_{MD} \approx 7$ min for the SD and MD reduc-

tion, namely, the 10.1% and 16.7% of the full model computational time. The largest part of the ROM computational effort is spent for the wave-basis extraction, which accounts approximately for 67% of total time for both the reductions. As a result, the SD reduction shows better performances than the MD one.

Conversely, when the user is interested in calculating the band structures along several directions of the IBZ, the MD reduction becomes a powerful tool to further enhance the computational savings. As a proof, we compare accuracy and computational time gains of SD and MD reductions through the whole IBZ by calculating the band structure along 11 directions $\theta_j = [0 : \pi/40 : \pi/4]$. As required by the methods, 11 collinear wave-basis are built for the SD reduction, while only 3 wave-basis at $\theta_d = [0 : \pi/8 : \pi/4]$ are constructed for the MD reduction.

Values of the minimal evanescence index E_{Ind} calculated using the SD and MD reductions are provided in the polar plots of Fig.7a and Fig.7b. We remark that evanescence index polar plots allow for an intuitive visualization of the directional wave attenuation properties of a periodic material. For example, one can quickly evaluate how the frequency width of the BGs depends on the chosen wave direction. In our case study, the second gap is a directional gap which disappears along specific directions within the IBZ.

Although useful, the construction of a polar plot within the whole IBZ can require a prohibitive computational time, especially when large models are analyzed or topology optimization are performed. For example, the polar plot calculated by means of the full (BOFEM) model would require > 7.0 hours (estimated from the single-direction calculation). This computational

time is drastically reduced, up to 10% of the full computational time, when the MD reduction is employed. In this example, the MD procedure allows a further computational time reduction of 67% with respect to the SD computational time (see data in Table 2). Together with the computational time gains, we also evaluate the relative errors between the SD and MD reductions by calculating the indices:

$$e_{k_r,rel}(\omega) = \max_n \left| \frac{k_{r,n}^{SD}(\omega) - k_{r,n}^{MD}(\omega)}{k_{r,n}^{SD}(\omega)} \right| \tag{24}$$

$$e_{E_{Ind,rel}}(\omega) = \left| \frac{E_{Ind}^{SD}(\omega) - E_{Ind}^{MD}(\omega)}{E_{Ind}^{SD}(\omega)} \right| \tag{25}$$

The values of the relative error $e_{k_r,rel}(\omega)$ as calculated within the whole IBZ considering the 11 directions $\theta = [0 : \pi/40 : \pi/4]$ and along the single generic direction $\theta_j = \pi/10$, are reported in Fig. 8a and b, respectively. The relative error $e_{k_r,rel}(\omega)$ is generally well below 10^{-2} within the whole IBZ. As expected, its value significantly drops ($\approx 10^{-5}$) along the direction $\theta_d = d \times \pi/8$, where the MD projection matrices are built. In this regard, one can refer to the average values of $e_{k_r,rel}(\omega)$ calculated within the IBZ and along two specific directions $\theta_j = \pi/10$, $\theta_j = \pi/4$, collected in Table 2. Similar trends are found for $e_{E_{Ind,rel}}(\omega)$ (see Table 2). Indeed, visual comparison between the evanescence index plots of Figs. 7a,b confirms that no significant discrepancy can be appreciated between the predictions provided by the two reductions.

4.2. Damped Plate

We evaluate the complex band structures of a damped aluminum stubbed plated to further discuss the accuracy and computational time saving of the

proposed ROM techniques. To this aim, a frequency independent (hysteretic) viscoelastic material model is assumed by means of a complex Young's modulus $E^* = E(1+i\eta)$ and a complex Poisson ratio $\nu^* = \nu(1+i\eta)$, with $\eta = 0.05$. The complex band structures are calculated again for 201 frequencies within the range 0-200 kHz along the direction $\theta_j = \pi/10$, employing the same mesh discretization of the previous example. First, some characteristics of a damped complex band structures are reviewed by discussing the results provided by the full model (black circles in Fig. 9). For a damped waveguide the distinction between purely propagative waves and evanescent/complex solutions vanishes since material dissipation yields a non-null attenuation across the whole frequency range (Figs. 9b,c). Hence, for the sake of clarity, Fig. 9a displays only the least decaying wave solutions with an evanescence index $E_{Ind} < 0.2$. As observed in literature for other damped waveguides (Moiseyenko and Laude, 2011), the introduction of material dissipation has major effects only on flat branches which disappear from the k_r vs. ω dispersion relation due to their high values of attenuation. The other branches of the band structure resemble the linear elastic ones (grey lines) across the whole frequency range of interest. Features typical of damped periodic waveguides are observed within the BG region where propagative branches are connected by "S-shaped" complex solutions.

Let us now discuss the accuracy and computational time saving achieved by the proposed ROM techniques. As for the linear elastic case, the SD and MD projection matrices are built following the procedure detailed in sect. 3. As a result, a projection matrix $\mathbf{P}(\mathbf{\Phi}_j)$ of 103 left-singular vectors along the direction $\theta_j = \pi/10$ and a projection matrix $\mathbf{P}(\mathbf{\Phi}_{0,1})$ of 208 left-singular

vectors along the directions $\theta_0 = 0$ and $\theta_1 = \pi/8$ are built, assuming a value of $\beta = 10^{-6}$ in the truncation criterion of Eq. (17). Again, excellent visual agreement between the prediction of the full and reduced models for both real and imaginary wavenumber components is found (see Figs. 9a,b). The same agreement characterizes the minimal evanescence index, plotted in Fig. 9c. An in depth quantitative analysis on the accuracy of the model reductions is performed employing the errors in Eqs.(22) and (23). Results for the error index in the real wavenumber prediction are displayed in Fig. 10a. Interestingly, slightly higher accuracy is found for the damped waveguide which shows values of e_{k_r} generally below 10^{-6} and below 10^{-3} for the SD and MD reduction, respectively. We remark that the error index e_{k_r} is calculated for a selection of least-decaying solutions with $E_{Ind} < 0.2$. As a result, flat branches characterized by large values of attenuation and prone to higher values of discrepancy are neglected, explaining the observed higher accuracy.

As observed for the linear elastic case, the SD reduction outperforms the MD reduction in terms of accuracy, nonetheless the MD predictions are still adequately accurate for analysis and design purposes. This observation is confirmed by the values of $e_{E_{Ind}}$ calculated along the direction $\theta = \pi/10$, which is now provided for the full range of frequencies 0-200 kHz (Fig. 10b). As regards to the computational time saving along $\theta = \pi/10$, the SD reduction requires 6% of the full computational time, while the MD reduction the 16.7%.

Finally, polar plots of the evanescence index as calculated using the SD and MD reduction are shown in Fig. 11a,b respectively, to summarize the

complex band structures calculation along the 11 directions $\theta = [0 : \pi/40 : \pi/4]$ within the IBZ. The polar plots highlight the effect of damping on the BG directionality, which is blurred by the intrinsic material dissipation. Focusing on the reduction accuracy, no visual disagreement is noticed between SD and MD predictions. This is quantitatively confirmed by the values of the relative error $e_{E_{Ind,rel}}$ calculated along the same directions $\theta = [0 : \pi/40 : \pi/4]$ and reported in Fig. 12a. The values of $e_{E_{Ind,rel}}$ are bounded below 10^{-2} within the whole IBZ with an average value $\approx 10^{-4}$ (see Table 3). As expected, the accuracy of the MD reduction increases along the direction $\theta_d = d \times \pi/8$, where the vectors are extracted. In this regards, one can compare the average values of $e_{E_{Ind,rel}}$ and $e_{E_{kr,rel}}$ calculated along the directions $\theta_j = 0$ and $\theta_j = \pi/4$ and collected in Table 3. The lower accuracy of the MD reduction is fully justified by its superior computational time savings ($\approx$ 58% with respect to the SD reduction) when the full IBZ is investigated (see Table 3).

5. Discussion

As remarked in Sect. 3, the proposed ROM technique exploits some numerical procedures, like sampling the cut-on and termination frequencies (Droz et al., 2014) and post-processing the Bloch modes via SVD (Boukadia et al., 2018), recently employed to reduce the computational effort of the WFEM. Indeed, WFEM-based ROM techniques can provide equally accurate complex band structures with time computational gains even larger than those observed in the proposed reduced BOFEM (Krattiger and Hussein, 2018; Boukadia et al., 2018).

However, the intrinsic performance of the WFEM approach largely depends on the direction where the complex band structure are sought. This occurs because the form of the EVP obtained by means of the WFEM changes in relation to the direction of wave propagation.

For sake of clarity, we here recall the general form of a WFEM EVP built along the direction $\theta = \tan^{-1}\frac{k_y}{k_x}$ for a generic 2D periodic material, as the one in Fig. 3a. According to the WFEM approach, once the two propagation constants $\mu_x = k_x a_x$ and $\mu_y = k_y a_y$ are identified, the form of the WFEM EVP depends on the ratio $r = \frac{\mu_y}{\mu_x}$.

When r is a rational number, we can set $\mu_x = bm_1$, and $\mu_y = bm_2$ (being b a constant), with m_1 and m_2 being integers with no common divisors. The EVP along the direction θ can thus be written as a polynomial of order $M = 2(m_1 + m_2)$ (Mace and Manconi, 2008):

$$\left[\sum_{j=0}^{j=M} \mathbf{A_j}\gamma^j\right]\mathbf{U} = \mathbf{0} \tag{26}$$

where $\mathbf{A_j}$ are dynamic matrices of dimensions $(n \times n)$, $\mathbf{U}$ is a vector $(n \times 1)$ of free displacements and $\gamma = e^{ib}$. Solutions $\gamma = e^{ib}$ of the EVP in Eq. (26) are found by linearization, leading to the system of equations:

$$\left(\begin{bmatrix}\mathbf{A_0} & & \\ & \mathbf{I} & \\ & & \ddots \\ & & & \mathbf{I}\end{bmatrix} - \gamma \begin{bmatrix}-\mathbf{A_1} & \dots & -\mathbf{A_{M-1}} & -\mathbf{A_M} \\ \mathbf{I} & & & \\ & \ddots & & \\ & & \mathbf{I} & \mathbf{0}\end{bmatrix}\right)\begin{bmatrix}\mathbf{U} \\ \gamma\mathbf{U} \\ \vdots \\ \gamma^{M-1}\mathbf{U}\end{bmatrix} = \mathbf{0} \tag{27}$$

The linearized EVP in Eq. (27) has dimensions $2nM \times 2nM$, i.e., M times larger than the linearized version of the BOFEM EVP in Eq. (8).

Conversely, when r is irrational, a nonlinear transcendental EVP is found. Such nonlinear EVP can be solved via root finding algorithms (e.g., the Newtons eigenvalue iteration method (Singh and Ram, 2002)). Nonetheless, iterative methods for large matrices are not only very time consuming, but require also a good initial guess to ensure convergence (Krattiger and Hussein, 2018).

Considering the numerical example in Sect. 4, Eq. (27) yields a $(2n \times 2n)$ system along the direction $\theta = 0$, a $(4n \times 4n)$ system, i.e., $m_1 + m_2 = 2$, along the direction $\theta = \pi/4$ and a $(22n \times 22n)$ system, along the direction $\theta = tan^{-1}(1/10)$, where the rational $r = \frac{m_2}{m1} = \frac{1}{10}$ is chosen to approximate the direction $\theta = \pi/40$ investigated with the BOFEM. Finally, we remind that computational algorithm utilized to solve EVPs can have different leading-order complexity, e.g, $O(N)$, $O(N^2)$, $O(N^3)$, with $N \times N$ being the dimensions the system, depending both on the type of solver (iterative or direct) and on the type of matrices (sparse or full) which characterized the system. Hence, a change in the system dimensions can significantly impact the computational effort required to solve the EVP.

These arguments suggest that the WFEM, and the related reduced versions, are the most suitable approaches when complex band structures along the IBZ boundaries are of interest. Conversely, the BOFEM approach, and the proposed ROM technique, may be preferred when one or multiple generic directions within the IBZ are investigated.

In this regards, we remark that although it is common practice to evaluate the band structures of complex materials simply along the boundaries of the IBZ, it is well demonstrated that this approach often do not suffice to

correctly locate band structure extrema (Harrison et al., 2007; Farzbod and Leamy, 2011). This is particularly true when low symmetry unit cells are investigated (Maurin et al., 2018). Such geometries, can easily result from topology optimization schemes designed to enlarge the BG width. Within this latter context, the presented reduction techniques can be fully exploited to reduce the burden of the computational cost preserving all the information coming from the full IBZ investigation.

6. Conclusions

In this work, a ROM technique able to accelerate the calculation of complex band structures along a generic direction within the unit cell IBZ has been presented and validated. The reduction employs a projection matrix which gathers a reduced set of left-singular vectors. These vectors are obtained from the SVD of a collection of propagative and evanescent Bloch modes. The Bloch modes are sampled at multiple cut-on and termination frequencies selected along purposely defined wave directions. In particular, when the basis direction coincides with that of the EVP formulation, a single-direction (SD) reduced model is obtained. Conversely, when two (or more) directions are chosen to collect the Bloch modes and form the wave-basis, a multi-direction (MD) reduced model is built.

The implementation of the method (in both its SD and MD versions) has been detailed for a generic 3D bi-periodic cell and validated via numerical examples discussing the dynamics of a periodic stubbed plate. Results demonstrate that the SD reduction provides accurate complex band struc-

tures with a computational time gain of one order of magnitude with respect to the standard BOFEM approach. Additionally, when MD reduced models are built, the computational time required to investigate the full IBZ is further reduced (up to $< 5\%$ of the full model computational time), still ensuring adequate accuracy for design and analysis purposes. Overall, the methodology appears suitable to reduce the computational effort required to assess the directional dispersive properties of complex periodic media.

Acknowledgments

A.P. acknowledges the support of the University of Bologna - DICAM through the research fellowship Metamaterials for seismic waves attenuation.

Table 1: Computational time and accuracy of SD and MD reductions for complex band structures calculation along $\theta = \pi/10$ - Linear elastic stubbed plate. The SD reduction is performed utilizing a wave basis constructed along the direction $\theta_d = \pi/10$, while the MD reduction combines two wave basis extracted along $\theta_d = [0, \pi/8]$. The computational times required for each step of the reductions and for the EVP solution are provided together with the average values of the error indices e_{k_r}, $e_{E_{Ind}}$.

		Computational Time				**Error**	
	N. dofs	**ω_c and ω_t Freq. Extr.**	**Basis Construction**	**EVP solution**	**Total**	**Ave. e_{k_r}**	**Ave. $e_{E_{Ind}}$**
Full model	13581	-	-	12.1x201= 2432 s	2432 s $\approx$ 40 min	-	-
SD Red. $\theta_d = [\pi/10]$	89	24 s	164 s	0.29x201= 58 s	246 s $\approx$ 4 min	0.00075 %	0.0045 %
MD Red. $\theta_d = [0, \pi/8]$	158	42 s	273 s	0.46x201= 92 s	407 s $\approx$ 7 min	0.016 %	0.044 %

Table 2: Relative computational time saving and accuracy of SD and MD reductions for complex band structures calculation within the IBZ at $\theta_j = [0 : \pi/40 : \pi/4]$ - Linear elastic stubbed plate. For the SD reduction 11 wave basis are constructed, one per each direction θ_j. For the MD reduction only 3 wave basis are extracted to form two projection matrices, one along $\theta_d = [0, \pi/8]$ for all $0 \leq \theta_j < \pi/8$, and one along $\theta_d = [\pi/8, \pi/4]$ for all $\pi/8 \leq \theta_j \leq \pi/4$. The computational times required for the EVP solution along the directions θ_j are provided together with the average values of the relative error indices $e_{k_r,rel}$, $e_{E_{Ind,rel}}$.

	Computational Time Reduction	**Relative Error**	
		Ave. $e_{k_r,Rel}$	**Ave.** $e_{E_{Ind,Rel}}$
MD vs. SD Red.	67% $t_{SDRed.}$ (10% t_{full})	0.088 % within the whole IBZ	0.197 % within the whole IBZ
		0.351 % for $\theta = \pi/10$	0.349 % for $\theta = \pi/10$
		0.0037 % for $\theta = \pi/4$	0.001 % for $\theta = \pi/4$

Table 3: Relative computational time saving and accuracy of SD and MD reductions for complex band structures calculation within the IBZ at $\theta_j = [0 : \pi/40 : \pi/4]$ - Damped elastic stubbed plate. For the SD reduction 11 wave basis are constructed, one per each direction θ_j. For the MD reduction only 3 wave basis are extracted to form two projection matrices, one along $\theta_d = [0, \pi/8]$ for all $0 \leq \theta_j < \pi/8$, and one along $\theta_d = [\pi/8, \pi/4]$ for all $\pi/8 \leq \theta_j \leq \pi/4$. The computational times required for the EVP solution along the directions θ_j are provided together with the average values of the relative error indices $e_{k_r,rel}$, $e_{E_{Ind,rel}}$.

	Computational Time Reduction	**Relative Error**	
		Ave. $e_{k_r,Rel}$	**Ave.** $e_{E_{Ind,Rel}}$
MD vs. SD Red.	58% $t_{SDRed.}$ (3.5% t_{full})	0.006 % within the whole IBZ	0.032 % within the whole IBZ
		0.004 % for $\theta = \pi/10$	0.055 % for $\theta = \pi/10$
		0.00029 % for $\theta = \pi/4$	0.00013 % for $\theta = \pi/4$

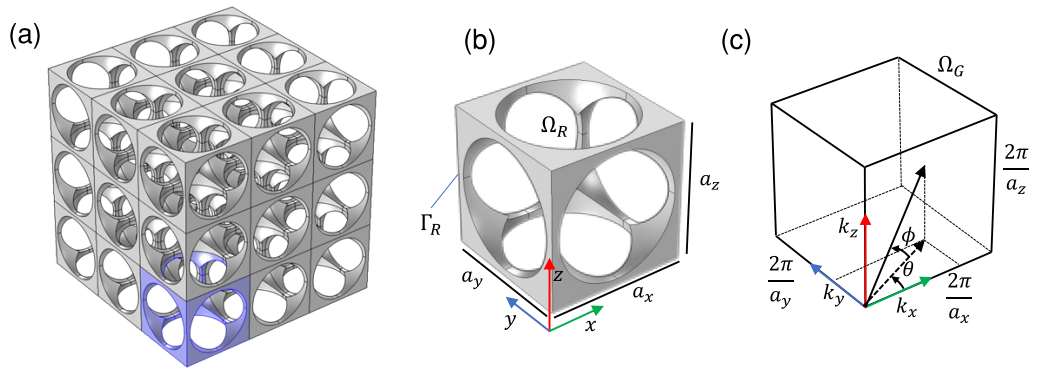

Figure 1: (a) Generic 3D periodic medium. (b) Unit Cell geometry. (c) Reciprocal lattice space.

References

Allemang, R.J., 2003. The modal assurance criterion–twenty years of use and abuse. Sound and vibration 37, 14–23.

Bloch, F., 1929. Über die quantenmechanik der elektronen in kristallgittern. Zeitschrift für Physik 52, 555–600. doi:10.1007/BF01339455.

Boukadia, R.F., Droz, C., Ichchou, M.N., Desmet, W., 2018. A bloch wave reduction scheme for ultrafast band diagram and dynamic response computation in periodic structures. Finite Elements in Analysis and Design 148, 1 – 12. doi:https://doi.org/10.1016/j.finel.2018.05.007.

Casadei, F., Rimoli, J., Ruzzene, M., 2013. A geometric multiscale finite element method for the dynamic analysis of heterogeneous solids.

615 Computer Methods in Applied Mechanics and Engineering 263, 56 – 70.
616 doi:https://doi.org/10.1016/j.cma.2013.05.009.

617 Casadei, F., Rimoli, J., Ruzzene, M., 2016. Multiscale finite element analysis
618 of wave propagation in periodic solids. Finite Elements in Analysis and
619 Design 108, 81 – 95. doi:https://doi.org/10.1016/j.finel.2015.10.002.

620 Collet, M., Ouisse, M., Ruzzene, M., Ichchou, M., 2011. Floquetbloch de-
621 composition for the computation of dispersion of two-dimensional periodic,
622 damped mechanical systems. International Journal of Solids and Struc-
623 tures 48, 2837 – 2848. doi:https://doi.org/10.1016/j.ijsolstr.2011.06.002.

624 Cracknell, A., 1974. Tables of the irreducible representations of the 17
625 two-dimensional space groups and their relevance to quantum mechani-
626 cal eigenstates for surfaces and thin films. Thin Solid Films 21, 107 – 127.
627 doi:https://doi.org/10.1016/0040-6090(74)90095-9.

628 Craig, R.R., Bampton, M.C.C., 1968. Coupling of Substruc-
629 tures for Dynamic Analyses. AIAA Journal 6, 1313–1319.
630 URL: https://hal.archives-ouvertes.fr/hal-01537654,
631 doi:10.2514/3.4741.

632 Droz, C., Lain, J.P., Ichchou, M., Inquit, G., 2014. A re-
633 duced formulation for the free-wave propagation analysis in
634 composite structures. Composite Structures 113, 134 – 144.
635 doi:https://doi.org/10.1016/j.compstruct.2014.03.017.

636 Droz, C., Zhou, C., Ichchou, M., Lain, J.P., 2016. A hybrid
637 wave-mode formulation for the vibro-acoustic analysis of 2d peri-

odic structures. Journal of Sound and Vibration 363, 285 – 302. doi:https://doi.org/10.1016/j.jsv.2015.11.003.

Duhamel, D., Mace, B., Brennan, M., 2006. Finite element analysis of the vibrations of waveguides and periodic structures. Journal of Sound and Vibration 294, 205 – 220. doi:https://doi.org/10.1016/j.jsv.2005.11.014.

Farzbod, F., Leamy, M.J., 2011. Analysis of Blochs Method and the Propagation Technique in Periodic Structures. Journal of Vibration and Acoustics 133. doi:10.1115/1.4003202. 031010.

Harrison, J.M., Kuchment, P., Sobolev, A., Winn, B., 2007. On occurrence of spectral edges for periodic operators inside the brillouin zone. Journal of Physics A: Mathematical and Theoretical 40, 7597–7618. doi:10.1088/1751-8113/40/27/011.

Hussein, M.I., 2009. Reduced bloch mode expansion for periodic media band structure calculations. Proceedings of the Royal Society A: Mathematical, Physical and Engineering Sciences 465, 2825–2848. doi:10.1098/rspa.2008.0471.

Hussein, M.I., Hulbert, G.M., 2006. Mode-enriched dispersion models of periodic materials within a multiscale mixed finite element framework. Finite Elements in Analysis and Design 42, 602 – 612. doi:https://doi.org/10.1016/j.finel.2005.11.002.

Hussein, M.I., Leamy, M.J., Ruzzene, M., 2014. Dynamics of Phononic Materials and Structures: Historical Origins, Recent Progress, and Future Outlook. Applied Mechanics Reviews 66. doi:10.1115/1.4026911. 040802.

Krattiger, D., Hussein, M.I., 2014. Bloch mode synthesis: Ultrafast methodology for elastic band-structure calculations. Phys. Rev. E 90, 063306. doi:10.1103/PhysRevE.90.063306.

Krattiger, D., Hussein, M.I., 2018. Generalized bloch mode synthesis for accelerated calculation of elastic band structures. Journal of Computational Physics 357, 183 – 205. doi:https://doi.org/10.1016/j.jcp.2017.12.016.

Krushynska, A., Kouznetsova, V., Geers, M., 2016. Visco-elastic effects on wave dispersion in three-phase acoustic metamaterials. Journal of the Mechanics and Physics of Solids 96, 29 – 47. doi:https://doi.org/10.1016/j.jmps.2016.07.001.

Kulpe, J.A., Sabra, K.G., Leamy, M.J., 2014. Bloch-wave expansion technique for predicting wave reflection and transmission in two-dimensional phononic crystals. The Journal of the Acoustical Society of America 135, 1808–1819. doi:10.1121/1.4864457.

Kushwaha, M.S., Halevi, P., Dobrzynski, L., Djafari-Rouhani, B., 1993. Acoustic band structure of periodic elastic composites. Phys. Rev. Lett. 71, 2022–2025. doi:10.1103/PhysRevLett.71.2022.

Laude, V., Achaoui, Y., Benchabane, S., Khelif, A., 2009. Evanescent bloch waves and the complex band structure of phononic crystals. Phys. Rev. B 80, 092301. doi:10.1103/PhysRevB.80.092301.

Laude, V., Moiseyenko, R.P., Benchabane, S., Declercq, N.F., 2011. Bloch wave deafness and modal conversion at a phononic crystal boundary. AIP Advances 1, 041402. doi:10.1063/1.3675828.

Mace, B.R., Manconi, E., 2008. Modelling wave propagation in two-dimensional structures using finite element analysis. Journal of Sound and Vibration 318, 884 – 902. doi:https://doi.org/10.1016/j.jsv.2008.04.039.

Maurin, F., Claeys, C., Deckers, E., Desmet, W., 2018. Probability that a band-gap extremum is located on the irreducible brillouin-zone contour for the 17 different plane crystallographic lattices. International Journal of Solids and Structures 135, 26 – 36. doi:https://doi.org/10.1016/j.ijsolstr.2017.11.006.

Moiseyenko, R.P., Laude, V., 2011. Material loss influence on the complex band structure and group velocity in phononic crystals. Phys. Rev. B 83, 064301. doi:10.1103/PhysRevB.83.064301.

Palermo, A., Marzani, A., 2016. Extended bloch mode synthesis: Ultrafast method for the computation of complex band structures in phononic media. International Journal of Solids and Structures 100-101, 29 – 40. doi:https://doi.org/10.1016/j.ijsolstr.2016.06.033.

Phani, A.S., Woodhouse, J., Fleck, N.A., 2006. Wave propagation in two-dimensional periodic lattices. The Journal of the Acoustical Society of America 119, 1995–2005. doi:10.1121/1.2179748.

Sigalas, M., Economou, E., 1993. Band structure of elastic waves in two dimensional systems. Solid State Communications 86, 141 – 143. doi:https://doi.org/10.1016/0038-1098(93)90888-T.

Sigalas, M., Kushwaha, M.S., Economou, E.N., Kafesaki, M., Psarobas, I.E., Steurer, W., 2005. Classical vibrational modes in phononic lattices: theory

and experiment. Zeitschrift für Kristallographie-Crystalline Materials 220, 765–809.

Singh, K.V., Ram, Y.M., 2002. Transcendental eigenvalue problem and its applications. AIAA Journal 40, 1402–1407. doi:10.2514/2.1801.

Wu, T.C., Wu, T.T., Hsu, J.C., 2009. Waveguiding and frequency selection of lamb waves in a plate with a periodic stubbed surface. Phys. Rev. B 79, 104306. doi:10.1103/PhysRevB.79.104306.

Wu, T.T., Huang, Z.G., Tsai, T.C., Wu, T.C., 2008. Evidence of complete band gap and resonances in a plate with periodic stubbed surface. Applied Physics Letters 93, 111902. doi:10.1063/1.2970992.

Zhou, C., Lain, J., Ichchou, M., Zine, A., 2015. Multi-scale modelling for two-dimensional periodic structures using a combined mode/wave based approach. Computers & Structures 154, 145 – 162. doi:https://doi.org/10.1016/j.compstruc.2015.03.006.

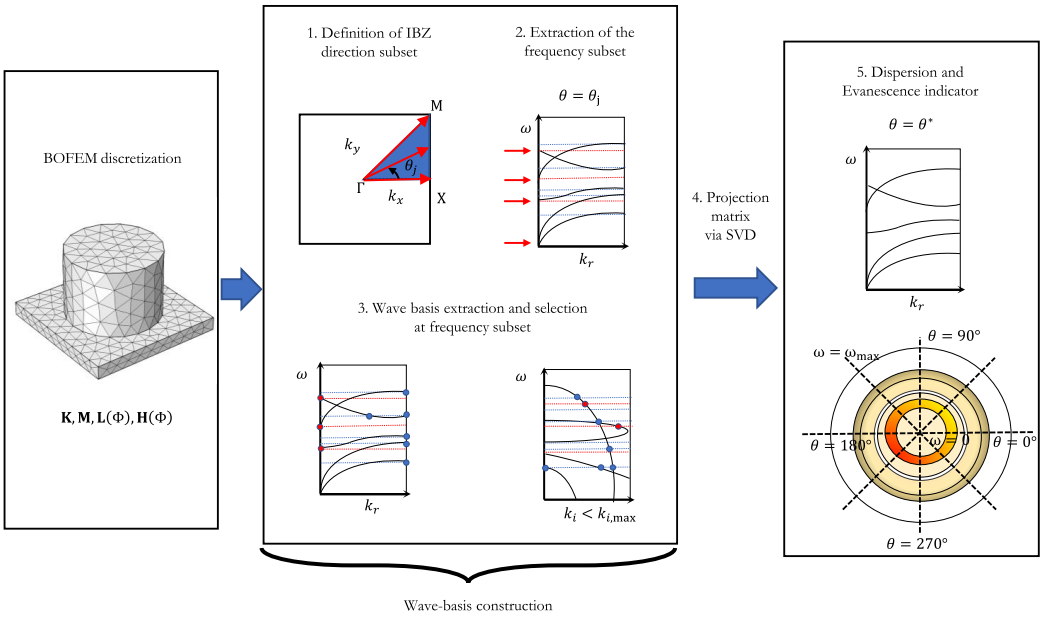

Figure 2: Schematic of the proposed ROM technique.

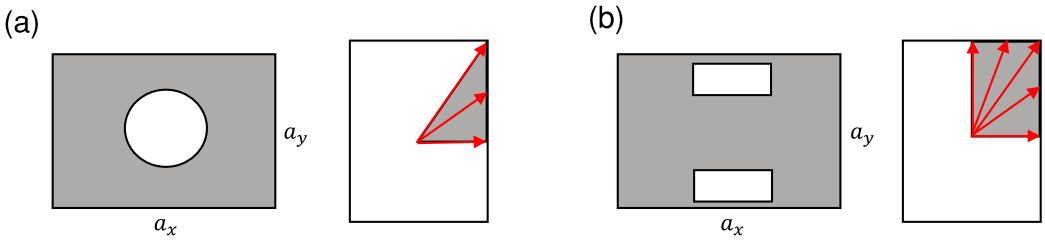

Figure 3: (a) High order (group symmetry p4mm (Cracknell, 1974)) and low order (group symmetry p1m1 (Cracknell, 1974)) bi-periodic unit cells and related First Brillouin Zones. Irreducible Brillouin Zones are highlighted in grey. Red arrows denote possible wave directions within the IBZ.

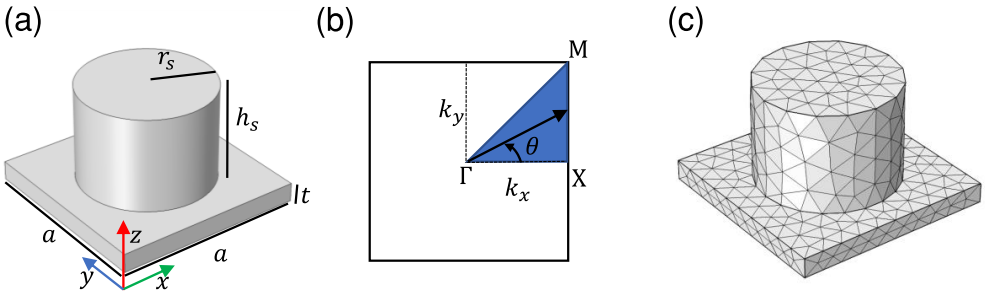

Figure 4: (a) Stubbed plate unit cell geometry. (b) Stubbed plate FBZ and IBZ. (b) Stubbed plate unit cell mesh.

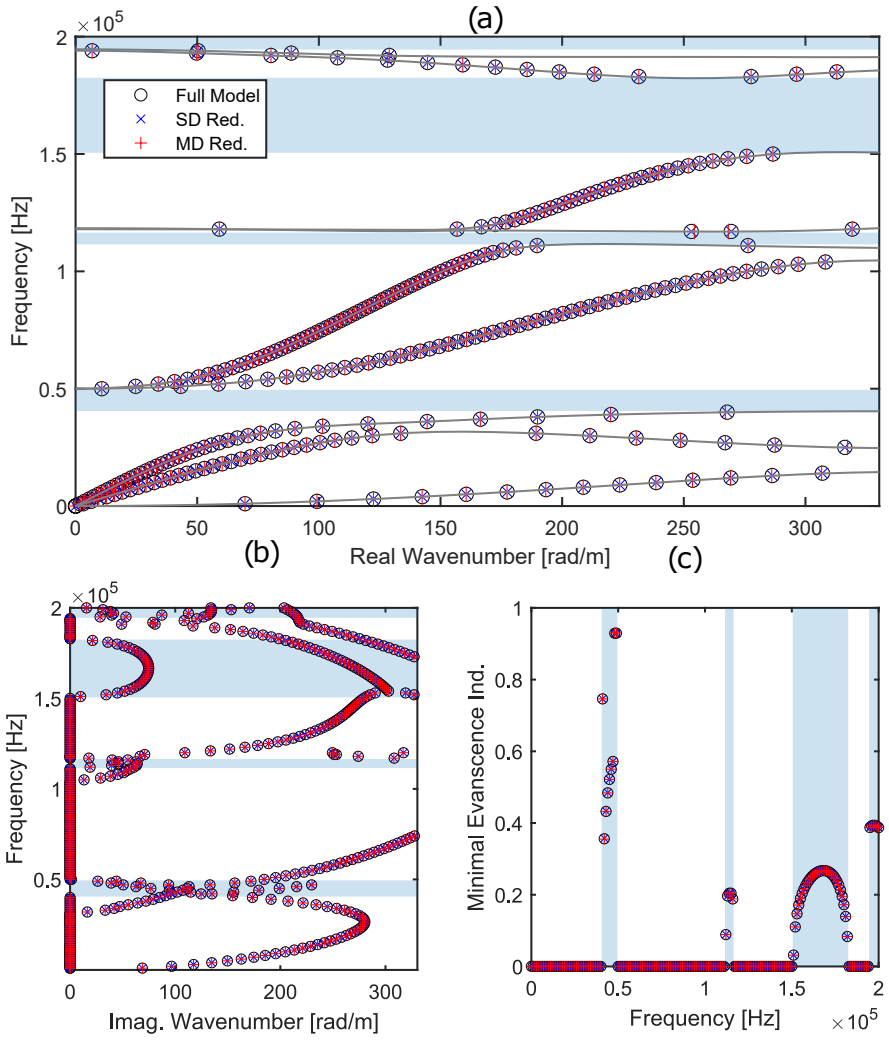

Figure 5: Linear elastic stubbed plate - Complex band structure along the direction $\theta = \pi/10$: (a) Propagative modes (k_r vs. freq.) and (b) Evanescent modes (k_i vs. freq.). (c) Minimal Evanescence Index (E_{Ind} vs. freq.).

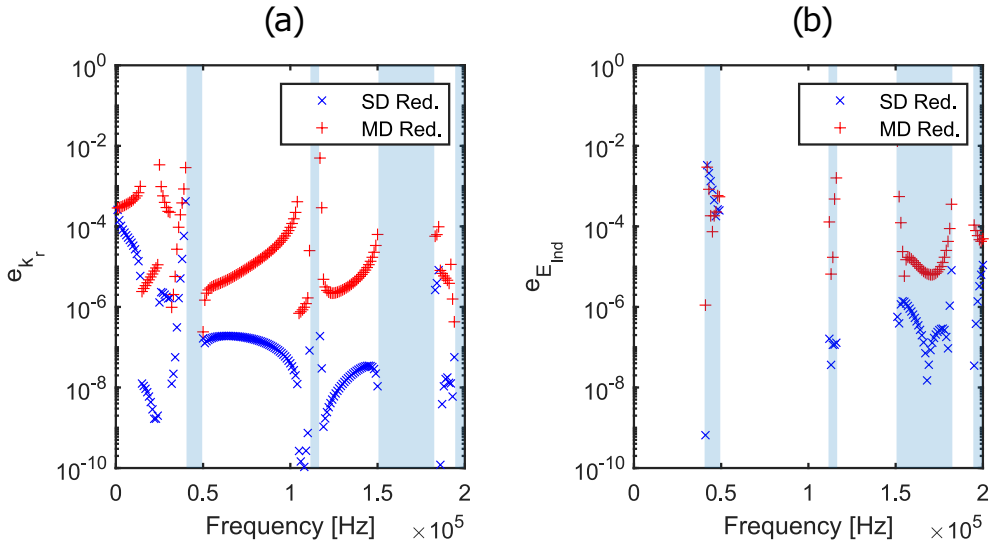

Figure 6: Linear elastic stubbed plate - Error analysis along the direction $\theta = \pi/10$: (a) Error e_{k_r} vs. freq. (b) Error $e_{E_{Ind}}$ vs. freq.

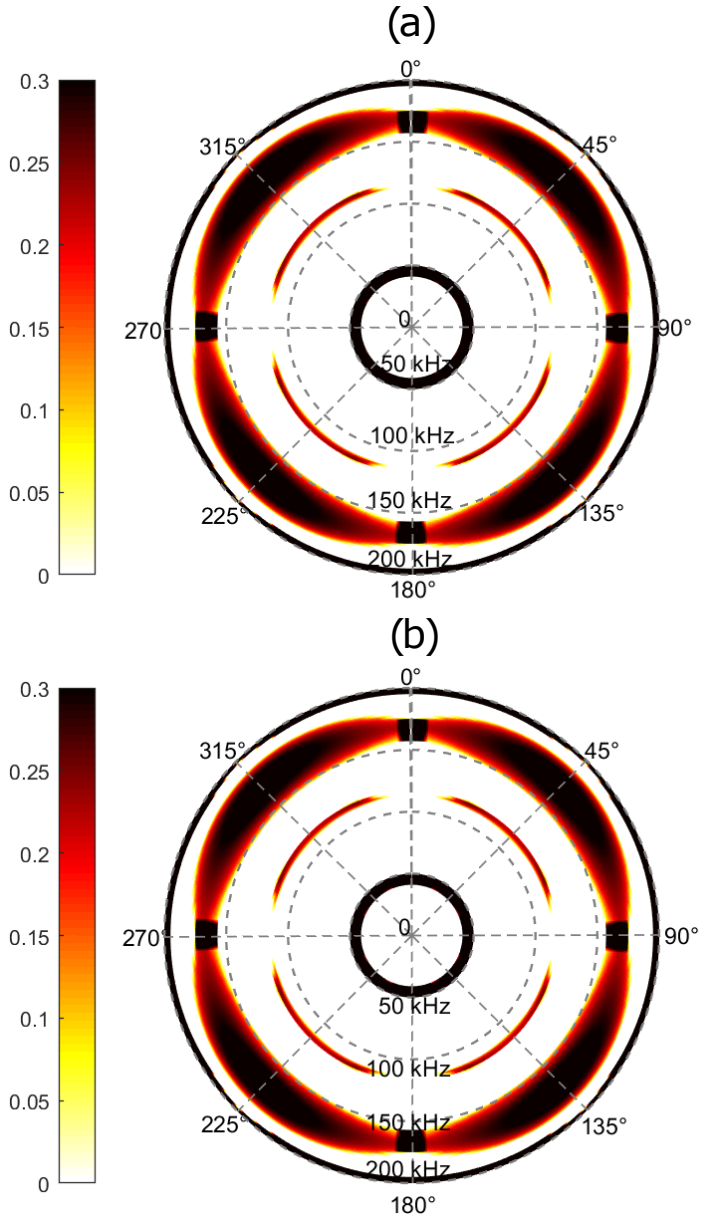

Figure 7: Linear elastic stubbed plate - Polar plot of the minimal evanescence index E_{Ind} calculated within the IBZ along the directions $\theta = [0 : \pi/40 : \pi/4]$. (a) SD reduction. (b) MD reduction.

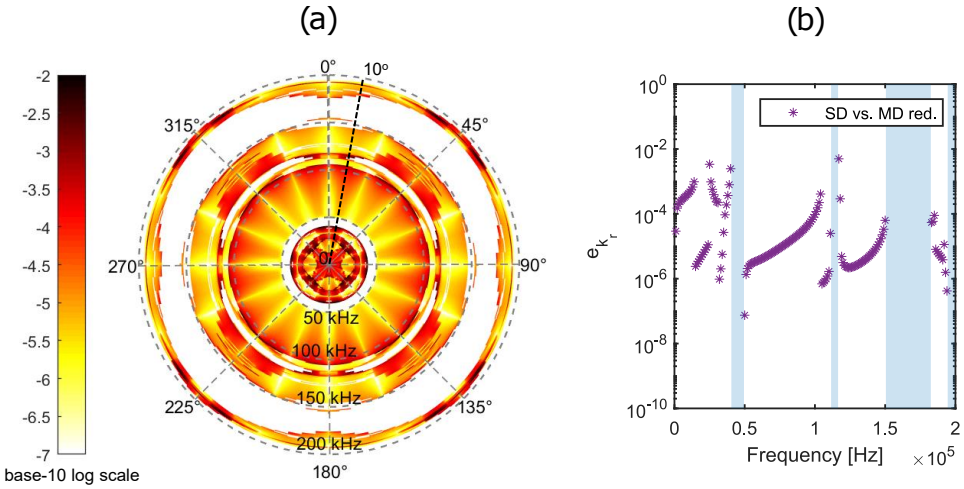

Figure 8: Linear elastic stubbed plate - Relative error analysis between SD and MD reductions. (a) Polar plot of the relative error $e_{k_r,rel}$ vs. freq. (calculated within the IBZ along the directions $\theta = [0 : \pi/40 : \pi/4]$). (b) Details of the relative error $e_{k_r,rel}$ vs. freq. along the direction $\theta = \pi/10$.

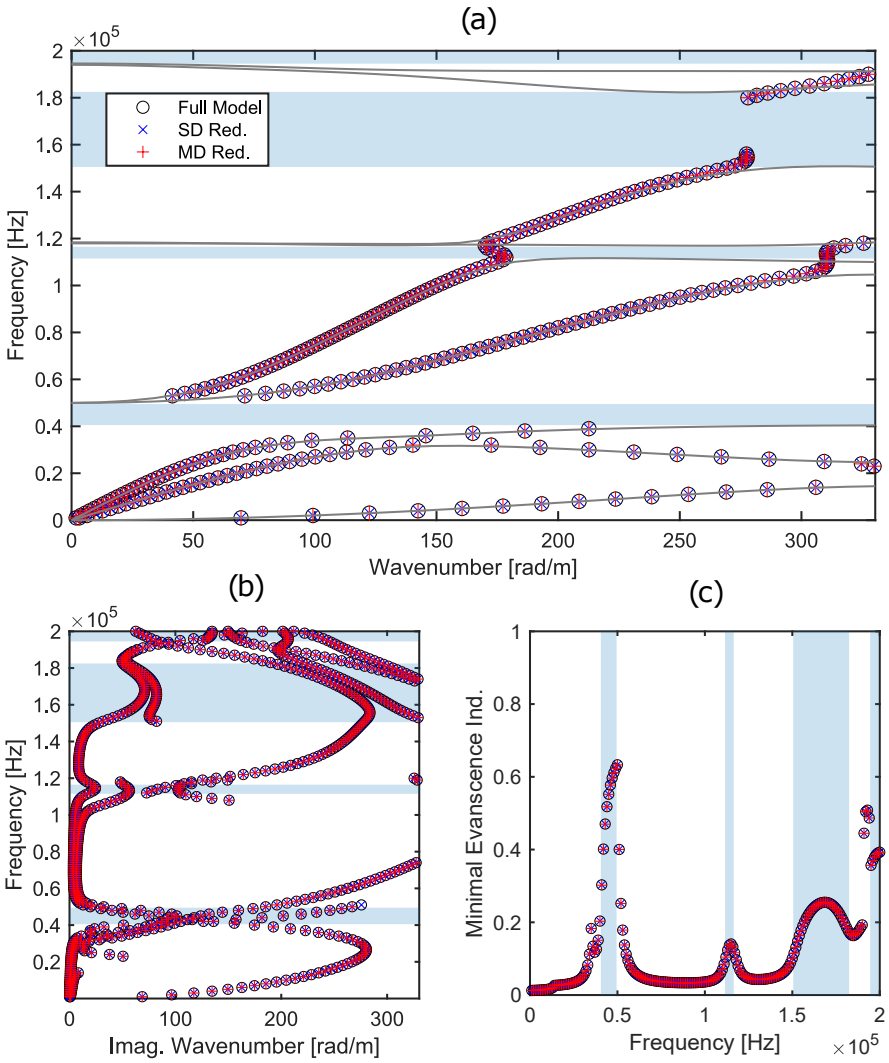

Figure 9: Damped elastic stubbed plate - Complex band structure along the direction $\theta = \pi/10$: (a) Least decaying modes (k_r vs. freq.). (b) Evanescent modes (k_i vs. freq.). (c) Minimal Evanescence Index (E_{Ind} vs. freq.).

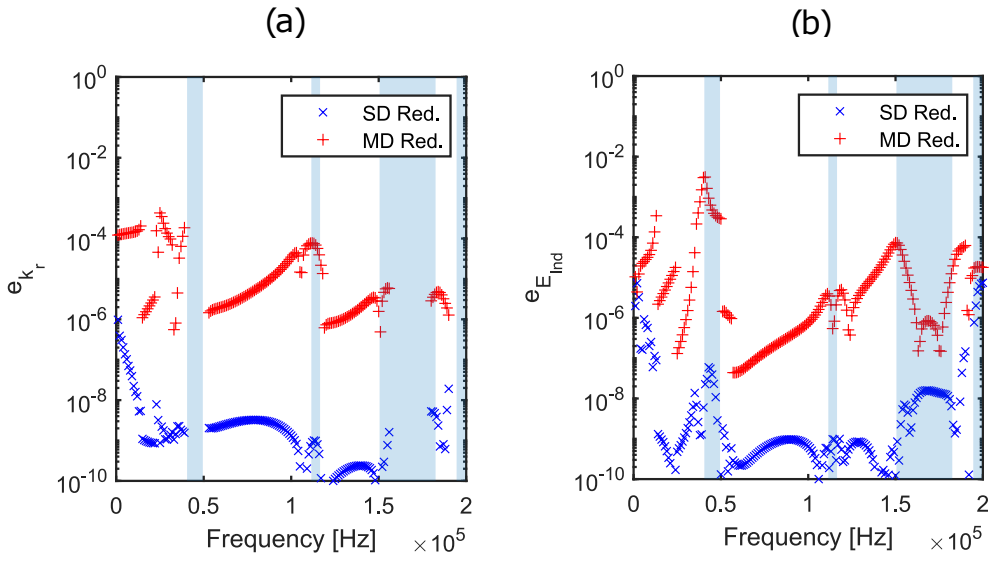

Figure 10: Damped elastic stubbed plate - Error analysis along the direction $\theta = \pi/10$: (a) Error e_{k_r} vs. freq. (b) Error $e_{E_{Ind}}$ vs. freq.

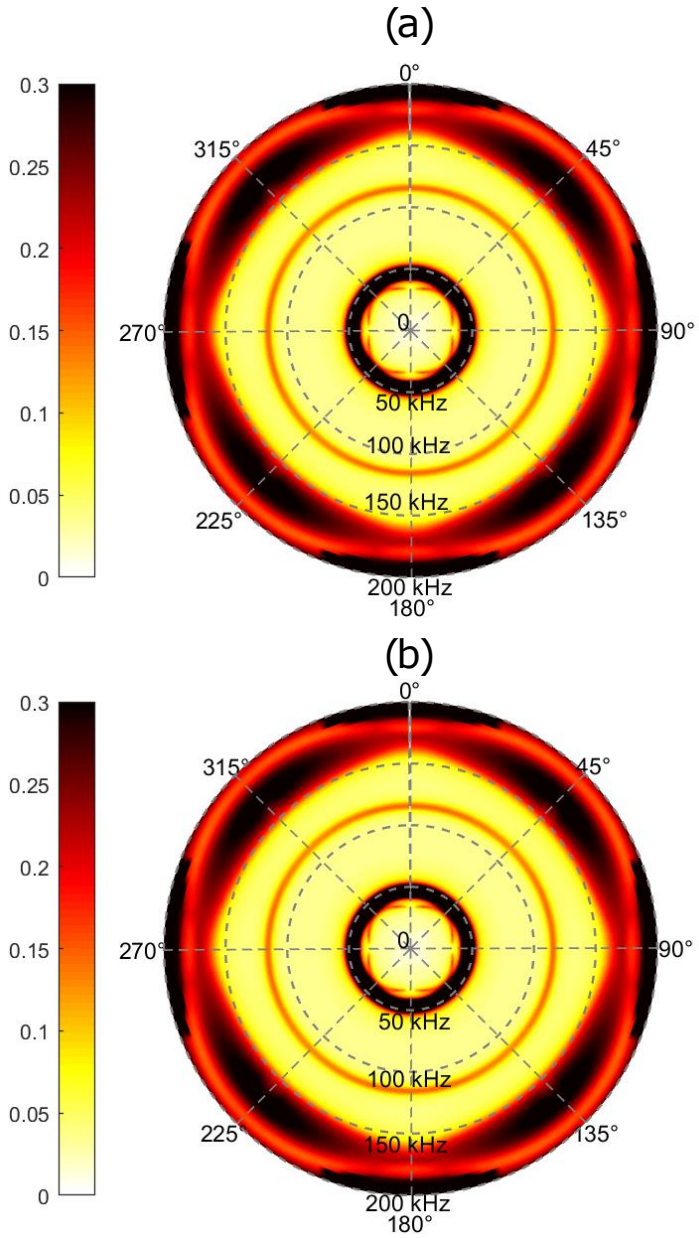

Figure 11: Damped elastic stubbed plate - Polar plot of the minimal evanescence index E_{Ind} calculated within the IBZ along the directions $\theta = [0 : \pi/40 : \pi/4]$. (a) SD reduction. (b) MD reduction.

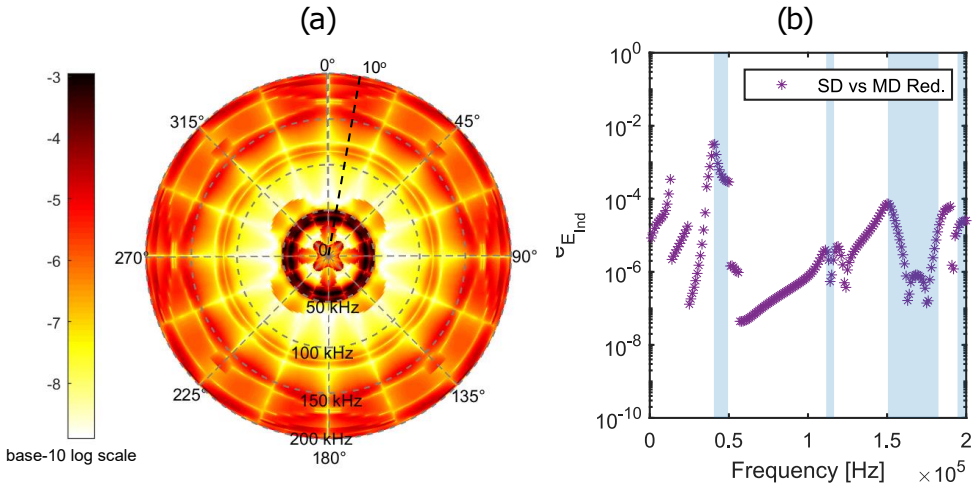

Figure 12: Damped elastic stubbed plate - Relative error analysis between SD and MD reductions. (a) Polar plot of the relative error $e_{Ind,rel}$ vs. freq. (calculated within the IBZ along the directions $\theta = [0 : \pi/40 : \pi/4]$). (b) Details of the relative error $e_{Ind,rel}$ vs. freq. along the direction $\theta = \pi/10$.